Journal of Global Positioning Systems (2025)
Vol. 21, Issue 2: 150-164
DOI:10.5081/jgps.21.2.150

A Method for Constructing Local Sea Surface Height Model in the South China Sea Using Dual-Source Spaceborne GNSS-R Data

Fanfan Xu[1,2,3], Baogui Ke[1,2,3,4], Jinxin Hu[4], Yuxuan Tan[1,2,3]

1. State Key Laboratory of Spatial Datum, Chinese Academy of Surveying and Mapping, Beijing 100036, China;
2. National Precise Gravity Measurement Facility, Huazhong University of Science and Technology, Wuhan 430074, China;
3. Beijing Fangshan Satellite Laser Ranging National Observation and Research Station, Beijing 100036, China;
4. Faculty of Geomatics, Lanzhou Jiaotong University, Lanzhou 730070, China

Abstract: Traditional satellite altimetry technology is well-established, yet it still faces limitations in spatiotemporal resolution. Currently, multiple Global Navigation Satellite System Reflectometry (GNSS-R) missions, with their distinct orbital configurations and revisit cycles, provide opportunities to enhance Sea Surface Height (SSH) retrieval capabilities through multi-source data fusion. To address the limitations of single GNSS-R data sources in terms of spatiotemporal coverage and retrieval accuracy, this study proposes a dual-source GNSS-R data fusion method based on wavelet transform. First, SSH is independently retrieved from CYGNSS (an 8-satellite constellation) and FY-3E (a single satellite) L1-band observations using a Delay-Doppler Map (DDM)-based physical retrieval algorithm, followed by the application of error correction models to mitigate systematic biases. Subsequently, leveraging the superior time-frequency localization characteristics of wavelet transform, the two datasets are fused to integrate valid signals and suppress noise. Based on this, a regional SSH model for the South China Sea was constructed. Validation using five months of in situ measurement data shows that the fused model achieves a Mean Absolute Error (MAE) of 0.93 meters for SSH retrieval. This result significantly outperforms traditional single-source GNSS-R physical retrieval methods, with a 48% improvement in accuracy compared to the CYGNSS single-satellite retrieval result (MAE = 1.78 m). This study demonstrates that by fusing multi-source GNSS-R data, the retrieval results outperform traditional single-source GNSS-R physical retrieval methods, thereby providing a complementary SSH dataset with unique observational advantages for regions such as the South China Sea, distinct from conventional radar altimetry.

Keywords: GNSS-R, DDM, Data fusion, Sea surface height

1. Introduction

Traditional Sea Surface Height (SSH) measurements rely primarily on tide gauges and satellite altimetry. Tide gauges provide long-term observational records but suffer from sparse spatial coverage; by contrast, conventional radar altimeters (e.g., the Jason series and Sentinel-6) deliver accurate measurements along their nadir tracks with near-global coverage, thus enabling large-scale monitoring of ocean dynamics. However, the limited spatial resolution of the trajectory may not be able to capture the more subtle or rapidly evolving ocean phenomena. In recent years, Global Navigation Satellite System Reflectometry (GNSS-R) has

Editors-In-Charge: Dr. C. K. Chum
Dr. Lei Yang

emerged as a complementary remote sensing technique. It leverages opportunistic signals from navigation satellites and retrieves SSH by measuring the time delay between the direct signal and the signal reflected off the sea surface. Currently, the accuracy of spaceborne GNSS-R based on single-frequency delay methods is typically limited to the meter level—constrained by factors such as single-frequency ionospheric delay, precise orbit determination errors, and instrument-related biases. Nevertheless, it boasts the advantages of dense spatial sampling and high revisit frequency, especially when deployed in constellations such as Cyclone Global Navigation Satellite System (CYGNSS). This unique sampling capability highlights the potential of GNSS-R to complement and enhance existing altimetry satellite missions[1-3].

Since Martin-Neira[4] first proposed the PARIS concept in 1993, GNSS-R technology has achieved remarkable progress in ocean altimetry. In 2016, Clarizia et al.[5] first validated the feasibility of spaceborne GPS-R for ocean SSH retrieval using six-month TDS-1 satellite data over the South Atlantic and North Pacific, with derived SSH maps showing general consistency but an 8.0 m RMSE(root mean square error) relative to the DTU10 model. Subsequently, Tian Luman et al.[6] achieved sub-meter accuracy in sea surface height measurements using Beidou reflection signals. In 2018, Mashburn et al.[7] analyzed global ocean surface datasets covering ±60° latitude from the TechDemoSat-1 (TDS-1) satellite, and reported a surface height residual of 6.4 m with a 1-s integration time, while also accounting for error sources such as orbit parameters, atmospheric delays, and tidal effects to assess the performance of spaceborne GNSS-R for ocean surface altimetry retrievals. By 2019, Li et al.[8] boosted the measurement accuracy to 3.9 m and 2.5 m via optimized re-tracking methods, based on raw CYGNSS data collected in the Gulf of Mexico, Caribbean Sea and western Atlantic from August 2017 to November 2018. In 2020, Mashburn et al. [9] proposed an improved delay re-tracking method and tested it on CYGNSS data over a region surrounding Indonesia (bounded by latitudes 25°S–20°N and longitudes 80°W–150°W), achieving a retrieval bias of approximately 6.0 m. That same year, Zhang Yun et al.[10] reduced the global mean absolute error of sea surface height retrieval to 6.05 m through error model optimization, using 20 consecutive days of L1B data from the TDS-1 satellite spanning April 10 to April 30, 2018, which represented a 29% accuracy improvement. Qiu et al.[11] reported that when using CYGNSS data from August 2017 and comparing the derived results with the DTU10 sea surface height model, the mean absolute error (MAE) reached 1.20 m and the root mean square error (RMSE) was 2.15 m. In 2022, Zhang et al.[12] adopted backpropagation (BP) and convolutional neural network (CNN) models for sea surface height (SSH) inversion using CYGNSS data, and the mean absolute errors (MAE) of the retrieved reflection point results from the two models over a 7-day period reached 1.04 m and 0.63 m, respectively, compared with the DTU18 model. In 2023, Cheng [13] et al. analyzed raw intermediate-frequency data from CYGNSS and TDS-1 satellites, optimizing altimetry accuracy to 2.38 m for GPS, 1.98 m for Galileo, and 1.91 m for Beidou. That same year, Zhang Yun [14] et al. utilized FY-3E GNOS-II data to demonstrate that Beidou retrieval achieved a maximum MAE of 3.0 m (outperforming GPS's 5.0 m) using physical and machine learning models, with random forest and CNN models reaching optimal MAEs of approximately 0.4 m. Despite these advances, a fundamental limitation persists: single-mission GNSS-R altimetry remains constrained by inherent trade-offs between spatial coverage, temporal sampling, and measurement precision. The CYGNSS constellation, with its dense coverage in the tropics, offers high spatiotemporal resolution but lacks truly global and homogeneous coverage. In contrast, polar-orbiting satellites like FY-3E provide more regular global coverage but with a coarser effective spatial sampling over a given region. This complementarity suggests that data fusion across missions could overcome the individual limitations of each system. Most recently in 2024, Zhang [15] et al.

developed a multilayer feedforward neural network model that achieved simulated altimetry accuracy of 0.07 m.

While single-mission GNSS-R altimetry has advanced significantly, its application is fundamentally constrained by inherent spatiotemporal sampling limitations. A single satellite system, whether a constellation like CYGNSS optimized for tropical coverage or a polar-orbiter like FY-3E, cannot simultaneously provide both high spatial density and continuous temporal coverage.The CYGNSS constellation provided high-density observations in tropical and subtropical regions. In contrast, the FY-3E satellite, with its focus on the Asia-Pacific region and global observational capability, offers complementary coverage and a different sampling pattern. To address the limitations of single GNSS-R data sources in terms of spatiotemporal resolution and coverage, Xing [16] et al. achieved an RMSE accuracy of 1.03 m by fusing CYGNSS and FY-3E observations through machine learning methods such as ANN (Artificial Neural Network) and IMM-KF (Interacting Multiple Model - Kalman Filter). However, these machine learning approaches cannot explicitly represent the underlying geometric–physical relationships. Therefore, this study adopts a physics-based retrieval approach that directly establishes deterministic physical relationships between SSH and DDM characteristic parameters by modeling the geometric interaction process between GNSS signals and the sea surface. Building upon the wavelet transform method's multiple advantages, including its multi-resolution analysis capability that adapts to varying sampling rates and data distributions, robust noise estimation performance that effectively mitigates disturbances from ionospheric delays and sea surface roughness, along with higher computational efficiency, we successfully constructed an SSH model for the South China Sea using five months of observational data. Experimental results show that the wavelet-based fusion of dual-source GNSS-R data yields higher accuracy than existing physics-based retrieval methods. The establishment of this model not only enables the effective application of multi-source GNSS-R data in marine geodesy, but also provides additional reference data for marine environmental monitoring.

2. Data

2.1 CYGNSS

The NASA Funded CYGNSS project was led by the University of Michigan and the Southwest Research Institute in the United States. It consists of eight 24 kg microsatellites operating in a low Earth orbit at an altitude of 510 km and an inclination of 35°. The signal sampling frequency is 1 Hz, and for a marine grid with a spatial resolution of 25 km, the average revisit cycle is approximately 7 hours[18]. Each satellite can simultaneously measure four reflectance bands. The system provides dense coverage of the tropical region between 38° north latitude and 38° south latitude (Figure 1), enabling the capture of mesoscale-ocean features that traditional altimetry satellites may overlook. CYGNSS has been continuously providing data in four product levels since March 18, 2017. This study utilizes publicly available Level 1 DDM data to derive sea surface height.

2.2 FY-3E

The FY-3E is a meteorological and navigation enhancement satellite jointly developed by the China Meteorological Administration and the National Space Administration. It has provided operational data since July 6, 2022. Operating in a sun-synchronous orbit at an altitude of 836 km and an inclination of 98.5°, the FY-3E GNOS-II has a revisit time of approximately 5 days [19], capable of receiving 8-channel reflected signals with a DDM sampling frequency of 1 Hz, covering the Asia-Pacific region and parts of the globe (Figure 2). The GNOS-II system onboard the satellite combines occultation detection and GNSS-R reflection detection capabilities, supporting the reception of signals from multiple systems, including China's Beidou Satellite Navigation System, the United

States' Global Positioning System, Russia's GLONASS, and the European Union's Galileo Satellite Navigation System. The data used in this paper is the FY-3E Global Navigation Satellite Occultation Detector L1 data (GNSS reflection), with the data product stored in HDF5 format

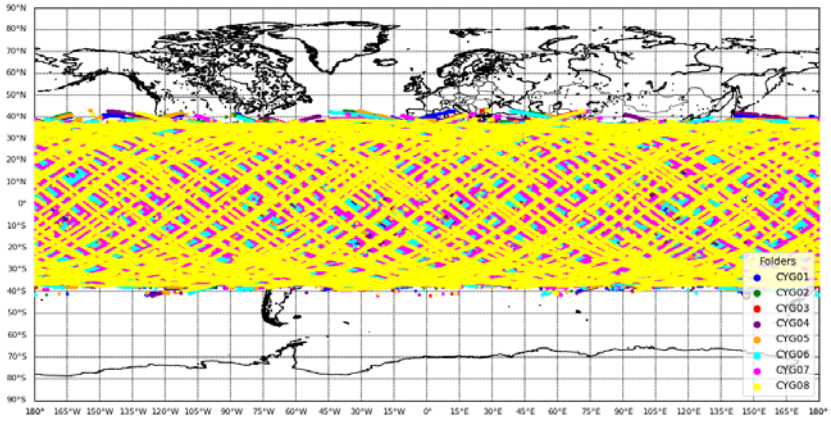

Fig.1 The spatial coverage tracks of the 8-satellite CYGNSS system in one day

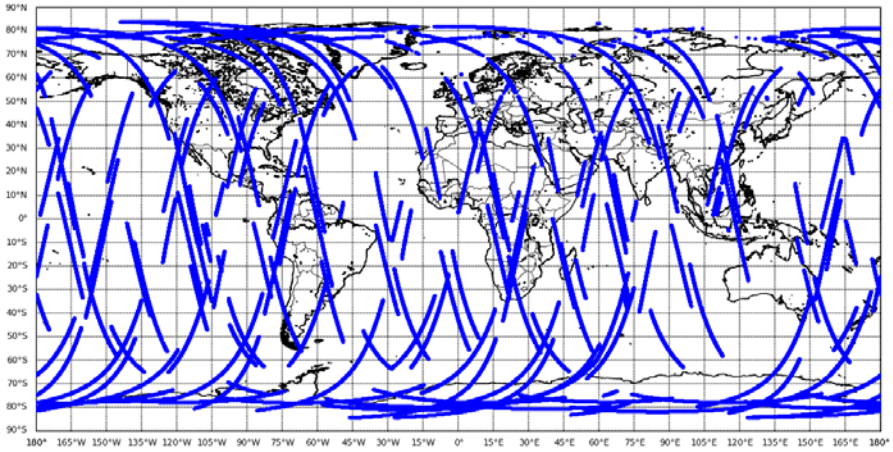

Fig.2 Daily spatial coverage trajectory of the FY-3E satellite

3. Methods

3.1 Re-tracking method

The maximum of its first derivative (DER) method[20] defines that the tracking point's delay must satisfy the following condition: The second derivative of the delay waveform M with respect to τ equals zero at $\tau = \tau_{spec}$, meaning the tracking point corresponds to the peak of the waveform's first derivative.

$$\frac{d^2W}{d\tau^2}\left(\tau_{spec}\right) = 0 \qquad (1)$$

The HALF Peak (HALF) method, derived from monostatic radar technology, determines the specular reflection delay by identifying a specific power ratio point of the peak-correlated waveform. Typically, the 75% power point [21] is adopted, as it approximates the theoretical optimal solution of the first-derivative method. Notably, when the ratio coefficient approaches 1 (i.e., the peak power point), the results become susceptible to sea surface roughness interference.

The Off Center of Gravity (OCOG)[22]

algorithm's core concept is to accurately determine the leading edge position of radar echo signals by calculating the optimal centroid position of the waveform, thereby retrieving surface elevation or sea surface height. Its implementation process consists of three key steps: First, the centroid position of the waveform is determined through multi-threshold energy distribution analysis; subsequently, under the constraints of maintaining constant centroid position and total area, the complex waveform is simplified into a rectangular box that shares identical centroid and area with the original waveform; finally, the waveform's amplitude A, width W and centroid position P are calculated. The re-tracking point position corresponds to the midpoint of the waveform's leading edge:

$$\tau = P - 0.5W \tag{2}$$

wherein P characterizes the centroid position, while W represents the effective width of the waveform.

3.2 Correction Models

3.2.1 Atmospheric Delay Error

The ionospheric delay correction utilizes the Global Ionosphere Model (GIM) published by the International GNSS Service (IGS). The coordinates of the piercing point are calculated, and the zenith total electron content at that location is obtained by interpolating the GIM data using the inverse distance weighting (IDW) method. Subsequently, based on the mapping function relationship, it is converted to the total electron content along the signal propagation path, ultimately determining the ionospheric delay along the signal path.

The ionospheric error correction reference method proposed by Yan et al.[23] , which approximates the ionosphere as a thin layer located 450 kilometers above the Earth's surface (the ionospheric single-layer model). The location where the signal penetrates this model is called the piercing point, whose coordinates are calculated by Equation (3) [24]:

$$\begin{aligned} \gamma &= \mathrm{A} - \arcsin\left(\frac{\mathrm{R} * \sin \mathrm{A}}{\mathrm{R}+\mathrm{H}}\right) \\ \varphi_m &= arcsin(\sin\phi_n \cos\gamma + \cos\phi_n \sin\gamma + \cos\alpha) \\ \lambda_m &= \lambda_n + arcsin(\frac{\sin\lambda \sin\alpha}{\cos\varphi_m}) \end{aligned} \tag{3}$$

where φ_m and λ_m denote the longitude and latitude of the piercing point, φ_n and λ_n represent the receiver's longitude and latitude, $\boldsymbol{A}$ is the satellite incidence angle, α indicates the satellite azimuth angle, γ is the geocentric angle, R stands for the Earth's radius, and H denotes the ionospheric single-layer height.

The core principle of inverse distance weighting (IDW) interpolation relies on the spatial correlation assumption that closer points exert greater influence. Mathematically, it calculates the distance between the interpolation point and surrounding known sample points, using the inverse distance (often raised to a power P) as the weighting coefficient—nearer points receive higher weights, while farther points are assigned lower weights. The final interpolated value is obtained by the weighted average of all known points' attribute values. The expression for the ionospheric piercing point in the zenith direction is as follows:

$$VTEC_{ion}^{j} = \begin{cases} \left(\sum_{i=1}^{n} \frac{VTEC_{ion}^{j}}{d_{ij}}\right) / \left(\sum_{i=1}^{n} \frac{1}{d_{ij}}\right), | \, d_{ij} < DR \\ VTEC_{ion}^{I}, | \, d_{ij} = 0 \end{cases} \tag{4}$$

where $VTEC_{ion}^{j}$ denotes the vertical total electron content value at the ionospheric piercing point j, $VTEC_{ion}^{I}$ represents the VTEC value at the ionospheric grid point i within the piercing point's coverage area, d_{ij} is the distance between the ionospheric piercing point j and the grid point i, and DR is the distance threshold[23].

For the same ionospheric layer, the total electron content (TEC) varies with direction. The TEC in the

desired direction is generally denoted as STEC, which represents the electron content along the signal path from the transmitter to the receiver. The conversion from VTEC to STEC is performed using a single-layer ionospheric projection function, expressed as follows [24]:

$$\begin{aligned} \mathrm{F}(\xi) &= \frac{\mathrm{STEC}}{\mathrm{VTEC}} = \frac{1}{\cos\xi} \\ \xi &= \arcsin\left(\frac{\mathrm{R}*\cos\theta}{\mathrm{R}+\mathrm{H}}\right) \end{aligned} \tag{5}$$

where ξ represents the angle between VTEC and STEC at the ionospheric piercing point, and θ denotes the satellite elevation angle.

The ionospheric delay is expressed as:

$$\rho_{ion} = \frac{40.3}{f^2} STEC \tag{6}$$

Tropospheric delay occurs when GNSS signals propagate through the neutral atmosphere. Due to the presence of gas molecules and water vapor in the atmosphere, the signal propagation speed decreases and the path bends, resulting in longer actual propagation time compared to vacuum conditions. This delay causes the GNSS-observed satellite geometric distance to be longer than the true distance. In this study, we employ the atmospheric delay model formula [25] for correction:

$$\rho_{tro} = \frac{4.6}{cosA}\left(1 - e^{\frac{H2}{8621}}\right) \tag{7}$$

3.2.2 Receiver Dynamic Error

This error is corrected using the model proposed by Hu [26]. Based on the model's assumption that a signal transmitted by the emitter at time t_0 is directly received by the receiver at t_1 and indirectly received at t_2, the path delay expression accounting for receiver dynamics is given by:

$$\rho_{mov} = \left\| GPS_{xyz}^{t_0} - SP_{xyz} \right\| + \left\| LEO_{xyz}^{t_2} - SP_{xyz} \right\| - \left\| GPS_{xyz}^{t_0} - LEO_{xyz}^{t_1} \right\| \tag{8}$$

The path delay neglecting receiver dynamics is expressed as:

$$\rho_{fix} = \left\| GPS_{xyz}^{t_0} - SP_{xyz} \right\| + \left\| LEO_{xyz}^{t_1} - SP_{xyz} \right\| - \left\| GPS_{xyz}^{t_0} - LEO_{xyz}^{t_1} \right\| \tag{9}$$

wherein GPS_{xyz} represents the transmitter position, LEO_{xyz} denotes the receiver position and SP_{xyz} indicates the specular reflection point position.

Consequently, the delay error induced by receiver dynamics can be expressed as:

$$\rho_d = \rho_{mov} - \rho_{fix} \tag{10}$$

3.3 Wavelet Transform Fusion Method

To address the fusion requirements of the dual-source satellite observation data from CYGNSS and FY-3E, this study employs a two-dimensional discrete wavelet transform (2D-DWT) to achieve multi-scale spatial feature separation. This method was selected due to the strong alignment between its mathematical properties and the challenges of dual-source data fusion. Specifically, the multi-resolution analysis capability of the wavelet transform is well-suited to leverage the complementary characteristics of the two datasets: CYGNSS offers high spatial sampling density over limited areas, while FY-3E provides global coverage with a coarser spatial resolution. Furthermore, the method's excellent noise-robust estimation performance allows it to accurately identify and effectively suppress spatially heterogeneous interference caused by ionospheric delay and sea surface roughness, thereby significantly enhancing the quality and reliability of the fused data.

The overall workflow of the proposed wavelet-based data fusion is illustrated in Figure 3. First, the original discrete observation data $I(x, y)$ is decomposed into a single layer. Specifically, each gridded data layer is then decomposed using a single-level 2D-DWT. This process involves applying

low-pass (ϕ) and high-pass (φ) filter kernels along the longitude (row) and latitude (column) directions, respectively, followed by down-sampling by a factor of 2. The decomposition yields four coefficient sub-matrices for each input layer:

cA (Approximation Coefficients): Contains the low-frequency components in both spatial directions.

cH (Horizontal Detail Coefficients): Captures high-frequency variations predominantly in the longitudinal (East-West) direction.

cV (Vertical Detail Coefficients): Captures high-frequency variations predominantly in the latitudinal (North-South) direction.

cD (Diagonal Detail Coefficients): Captures high-frequency variations in both directions simultaneously, often associated with fine-scale details and noise.

Meantime, low-pass (ϕ) and high-pass (φ) filtering operations are performed on the longitude (row direction) and latitude (column direction), respectively:

$$\begin{cases} \mathrm{cA} = \phi_{\mathrm{col}} * (\phi_{\mathrm{row}} * \mathrm{I}) \\ \mathrm{cH} = \varphi_{\mathrm{col}} * (\phi_{\mathrm{row}} * \mathrm{I}) \\ \mathrm{cV} = \phi_{\mathrm{col}} * (\varphi_{\mathrm{row}} * \mathrm{I}) \\ \mathrm{cD} = \varphi_{\mathrm{col}} * (\varphi_{\mathrm{row}} * \mathrm{I}) \end{cases} \tag{11}$$

The operator $*$ denotes the convolution operation, where ϕ and φ represent the scaling function and wavelet function, respectively. Through down-sampling, the size of each coefficient matrix is halved, reducing computational complexity while retaining multi-resolution characteristics.

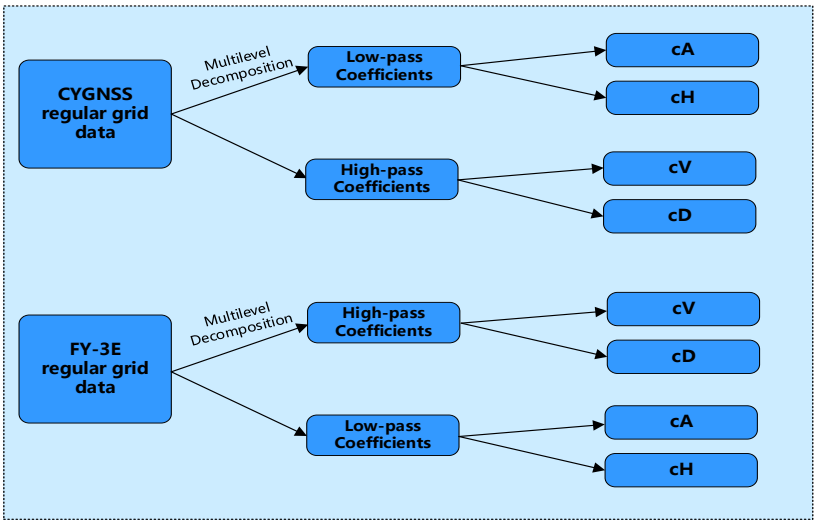

Fig.3 Wavelet decomposition example diagram

For the low-frequency approximation coefficients, a weighted averaging method is employed to fuse the dual-source data, enhancing the stability of the fusion results. For the high-frequency detail coefficients, an absolute maximum selection method is adopted to strengthen edge and texture features. Finally, the fused coefficients are reconstructed into high-resolution sea surface height grid data through a 2D inverse discrete wavelet transform. The advantage of this method lies in its effective separation of signal and noise through wavelet multi-scale decomposition, combined with physically constrained fusion rules. It improves spatial continuity while preserving fine-scale satellite observation characteristics, providing high-precision input for subsequent sea surface height inversion.

3.4 Accuracy Validation

DTU21 (DTU Mean Sea Surface 21), developed by the Technical University of Denmark [27], is a globally recognized high-precision and high-resolution mean sea surface model widely

validated in scholarly research [10, 28, 29]. In this study, DTU21 serves as the benchmark reference to evaluate the inversion accuracy of spaceborne sea surface height measurements using the following metrics:

$$MAE = \frac{1}{n}\sum_{i=1}^{n}(|SSH_i - DTU_i|)$$
$$RMSE = \sqrt{\frac{1}{n}\sum_{i=1}^{n}(SSH_i - DTU_i)^2} \quad (12)$$
$$R = \frac{\sum_{i=1}^{n}(SSH_i - \overline{SSH}) - (DTU_i - \overline{DTU})}{\sqrt{\sum_{i=1}^{n}(SSH_i - \overline{SSH})^2 \sum_{i=1}^{n}(DTU_i - \overline{DTU})^2}}$$

4. Analysis and Discussion

4.1 Sea Surface Height Retrieval Using Single-Satellite Data

The CYGNSS raw dataset was initially filtered using the parameter thresholds specified in Table 1, which were established based on the data quality control methodology outlined in Reference 10. For the FY-3E data, while applying the same quality control criteria from Table 1, additional screening conditions were implemented to detect and remove waveform anomalies in the DDM data, thereby effectively eliminating blank data and invalid observations with poor quality. To ensure data consistency and simplify the analysis of inter-system biases within this initial fusion framework, this study selected the GPS L1 C/A signal as the primary data source for FY-3E. This choice aligns with the signal type used by CYGNSS, thereby establishing a common technical foundation for subsequent cross-mission data fusion. During the data preprocessing stage, waveform slices corresponding to zero Doppler frequency were extracted from the DDM [30], followed by linear normalization and cubic spline interpolation.

Tab 1. Quality Control Standards for Low Earth Orbit (LEO) Satellite Data

Parameter	Screening Conditions
Incidence Angle	< 40 °
SNR	> -5 dB
Antenna Gain	> 5 dB
Satellite Status	= 0
Quality Flags	= 0

This study utilized CYGNSS and FY-3E satellite observation data from August 1, 2022. The raw datasets were first subjected to quality screening and preprocessing. To improve the accuracy of the inversion results, the sea surface height data obtained from the inversion was processed using the error correction model constructed in the previous section.The sea surface height retrieval process using GNSS-R is affected by various error sources. Existing studies indicate that ionospheric delay, tropospheric delay, and reflection signal delay are the three most dominant errors, with magnitudes reaching up to 15 m, 7 m, and 10 m, respectively[10]. To address these dominant errors, a corresponding error correction model has been developed in this study. Table 2 presents the evaluation results of single-track data from the CYGNSS and FY-3E satellites after error correction. A comparative analysis with reference data from the DTU model shows that the sea surface height retrieval accuracy of both types of satellites is significantly improved after error correction. Systematic experimental validation further demonstrates that the proposed model can enhance the overall retrieval accuracy by 7–9 meters, fully verifying its effectiveness and reliability.

Tab 2. Error Correction Results of Sea Surface Height Inversion for the Two Types of Satellites

	MAE of initial sea level /m	MAE after error correction /m
CYGNSS	14.23	4.37
FY-3E	7.71	1.76

Subsequently, three DDM waveform re-tracking algorithms—DER, HALF, and OCOG—were applied for sea surface height retrieval. Selecting DER as the optimal algorithm for this study is justified not only by its superior numerical accuracy but also due to its inherent physical advantages. To evaluate the algorithm accuracy, the retrieved SSH results were

compared with the DTU model, and the mean absolute error for each re-tracking method was calculated. Figure 4 presents the waveform experimental results derived from CYGNSS and FY-3E data, respectively. Significant differences in measurement precision were observed among the re-tracking algorithms, as summarized in Table 3. Consistent with expectations based on physical principles, DER's physical mechanism of determining the specular point delay by analyzing the derivative (rate of slope change) of the waveform leading edge makes it particularly robust against waveform distortions caused by moderate to rough sea states. In contrast, the HALF algorithm, which assumes an idealized waveform shape, and the OCOG algorithm, which is sensitive to the overall waveform center of gravity, are more susceptible to errors under such dynamic ocean conditions. The DER algorithm achieved an MAE reduction of approximately 15%–20% compared to the other two methods. Therefore, this comparative analysis, which combines performance metrics and physical interpretation, provides critical justification for selecting DER as the optimal re-tracking algorithm and offers a reference direction for optimizing GNSS-R SSH inversion algorithms in complex marine environments.

Tab 3. Accuracy Comparison of Two Satellite Datasets Using Different Retracking Methods Before and After Error Correction

	DER /m	DER-Cor/m	HALF /m	HALF-Cor/m	OCOG /m	OCOG-Cor/m
CYGNSS	14.23	4.38	16.25	11.07	21.85	9.47
FY-3E	7.71	1.76	10.63	5.77	11.36	7.49

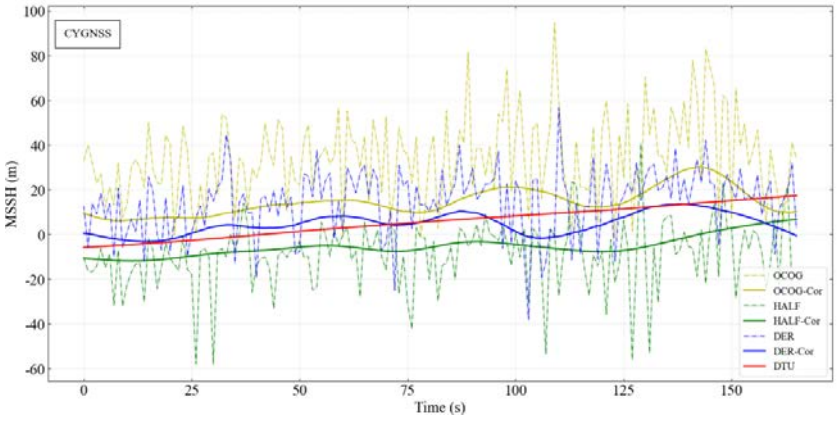

（a）

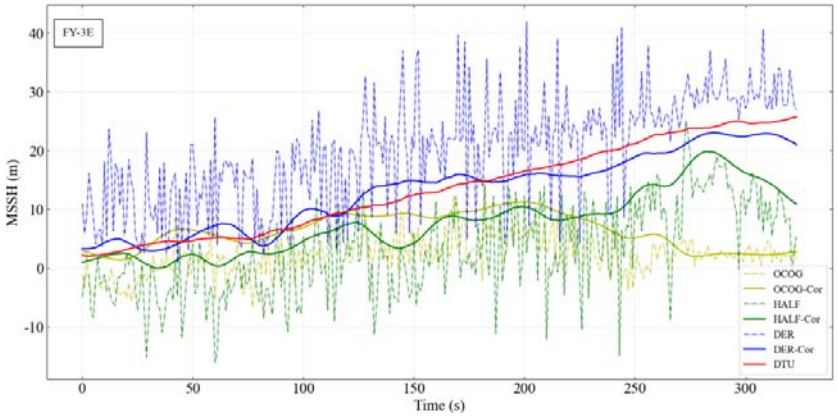

(b)

Fig.4 Analysis of inversion results based on different re-tracking methods

(a) Comparison of methods for CYGNSS; (b) Comparison of methods for FY-3E

By comparing the average absolute error results of three re-tracking methods, this study ultimately adopted the DER re-tracking method for sea surface height inversion.

4.2 South China Sea Local SSH Inversion via Wavelet-Based Fusion Algorithm

The experiment selected data from August 1, 2022, to December 31, 2022. The study area is located between 110° and 114° east longitude and 14° and 18° north latitude. The selection of this region was based on two key considerations: (1) the sea state in this area was relatively calm during the study period, providing a favorable signal environment for GNSS-R observations; (2) the region is covered by overlapping tracks from multiple reference altimetry missions such as Jason-3 and Sentinel-6, which can supply a sufficient number of high-precision, spatiotemporally matched co-located data points to support robust validation analysis. Since the FY-3E satellite began providing data on July 6, 2022, selecting the period after August ensures the stability of data quality. Additionally, this period falls during the transition from the late summer monsoon to the early winter monsoon in the South China Sea, characterized by relatively calm sea conditions. This effectively avoids the high-impact periods of strong monsoons and typhoons, significantly reducing the scattering interference caused by sea surface roughness on GNSS-R signals. This study period lays the foundation for future efforts to construct high-precision, high-stability sea surface height models using long-term GNSS-R observation data. The distribution of experimental data is shown in Figure 5.

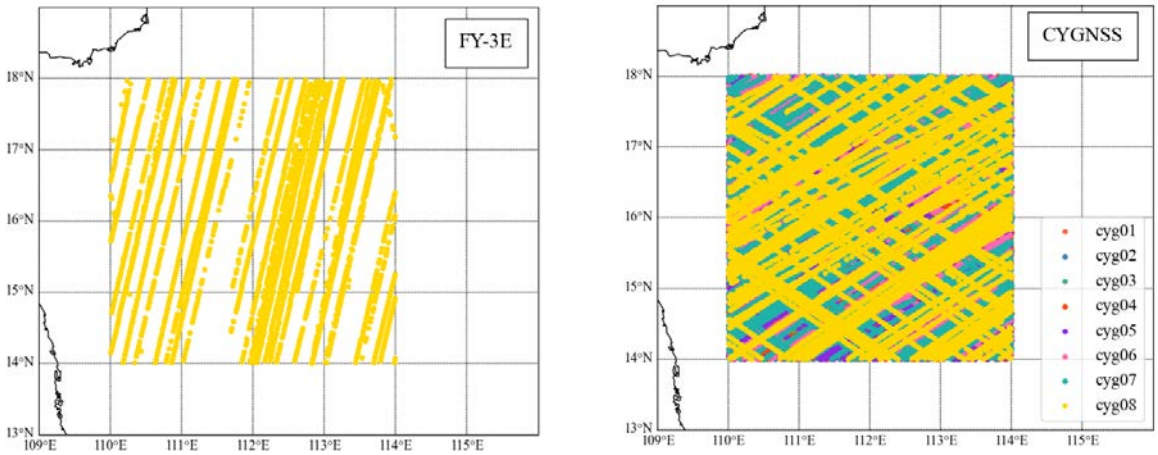

（a）FY-3E satellite data （b）CYGNSS satellite data

Fig.5 Spatial distribution and volume of experimental data

Based on the above experimental results, the impact of wavelet basis function selection on data fusion performance was further investigated, and the fusion experimental results of four wavelet basis functions - Haar, Db4, Coif3, and Sym5—were compared. The research results indicate that the Haar wavelet basis function achieves superior sea surface height inversion accuracy compared to the other three functions. The mean absolute error of sea surface height inversion for each wavelet basis function is shown in Table 4. Especially in large-scale real-time data processing scenarios, the Haar wavelet, due to its simple mathematical form and fast computational capabilities, can efficiently complete sea surface height fusion tasks. Therefore, it was selected as the core wavelet basis function for the experiments in this paper.

Tab.4 Accuracy Evaluation of Fusion Results Using Different Wavelet Basis Functions

Wavelet Basis Functions	MAE /m
Haar	0.93
Db4	1.02
Coif3	0.94
Sym5	0.98

To further optimize the fusion performance of CYGNSS and FY-3E satellite data, a weighting ratio experiment was designed based on the characteristic differences between the two data sources. Considering the higher spatio-temporal resolution advantage of CYGNSS data, the experiment set up five weighting schemes of 10%, 30%, 50%, 70%, and 90% for systematic comparison. The experimental results in Table 5 indicate that a 1:1 fusion ratio achieves the peak accuracy in sea surface height retrieval. This verifies the distinct complementarity between the FY-3E and CYGNSS datasets. The balanced fusion successfully consolidates their respective advantages, leading to a holistic optimization of retrieval efficacy.

To construct a sea surface height model with as uniform data distribution as possible, the study area was spatially divided into 3′×3′ grids, and the data fusion method proposed in the preceding section was used to integrate the data. This grid resolution effectively preserves the spatial detail characteristics of CYGNSS and FY-3E satellite data while ensuring computational efficiency. The inversion data from CYGNSS and FY-3E satellites are interpolated into the same grid system using a Gaussian kernel function. A single-layer decomposition is performed on the dual-source data using Haar wavelet bases, with low-frequency coefficients fused using a weighted average method and high-frequency coefficients selected using the absolute maximum value method; finally, the fused high-resolution grid data of the sea surface is reconstructed through inverse wavelet transformation.

Tab.5 Performance Comparison of Fusion Algorithms under Varied Wavelet Coefficient Weightings

CYGNSS weighting / %	MAE /m
10	1.97
30	1.37
50	0.93
70	1.02
90	1.45

Fig.6 Wavelet transform fusion results

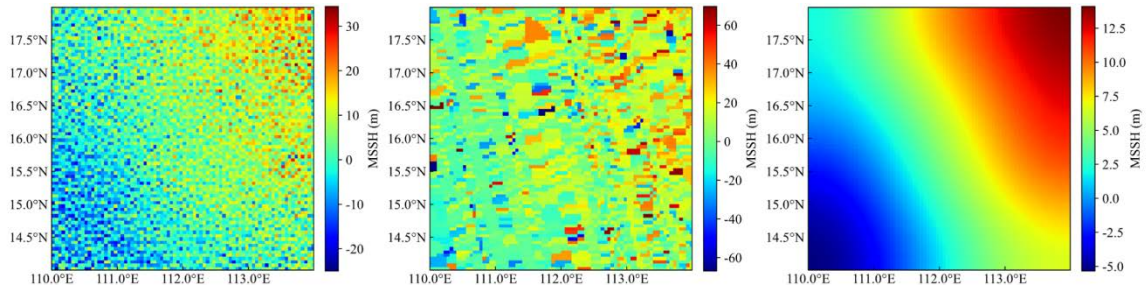

(a) (b) (c)

(a) Sea surface height retrieval results from CYGNSS data;(b) Sea surface height retrieval results from FY-3E data;(c) Sea surface height results obtained through wavelet transform fusion of CYGNSS and FY-3E datasets

The sea surface height results obtained from inversion were compared and analyzed with the DTU global model. First, the inverse distance weighted interpolation method was used to calculate the sea surface height reference values of the DTU model in the study area. Subsequently, the mean absolute errors between each satellite data source and the reference model were calculated. The statistical results in Table 6 show that the MAE for both the FY-3E satellite and CYGNSS single-satellite data exceeds 3 m. However, after fusing the data from the 8 satellites in the CYGNSS system, the MAE significantly decreases to 1.78 m. This result validates the advantage of data fusion in improving inversion accuracy. Based on this finding, the results of further experiments on dual-source data fusion between FY-3E and the CYGNSS system are shown in Figure 7. The fusion improved the sea surface height inversion accuracy to the decimeter level compared to single-satellite data. This achievement indicates that the South China Sea local sea surface height model constructed through dual-source satellite data fusion has higher inversion accuracy than traditional physical inversion methods relying on single-satellite data.

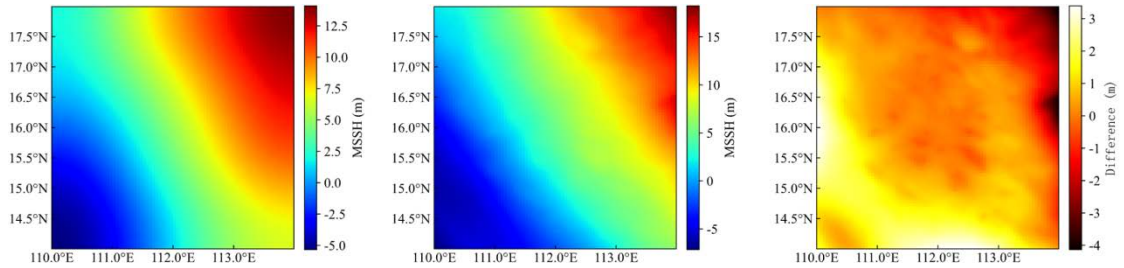

(a) (b) (c)

Fig.7 Comparison of fused sea surface height results. (a) Sea surface height from dual-source data integration; (b) DTU model; (c) Difference between the integration result and the DTU model

Tab.6 Comparison of Mean Absolute Errors Between Different Satellite Altimetry Data and the DTU Model

Data source	Satellite Status	MAE /m	RMSE /m	R
FY	Single-Satellite	3.88	4.39	0.78
CYG01	Single-Satellite	4.41	5.64	0.75
CYG01-CYG08	Homogeneous Constellation Fusion	1.78	2.19	0.99
CYG01-CYG08+FY	Heterogeneous Constellation Fusion	0.93	1.26	0.99

5. Conclusion

This study developed a regional sea surface height model for the South China Sea (110°–114° E, 14°–18° N) using approximately five months of spaceborne GNSS-R observations from both the CYGNSS and FY-3E satellites. During the single-satellite data inversion phase, the DER algorithm within the GNSS-R single-point retracking method was employed to process CYGNSS and FY-3E data separately, and a systematic error correction model was established. This effectively mitigated major error sources such as ionospheric delay, tropospheric delay, and reflected signal delay, thereby significantly improving the accuracy of SSH inversion by 7–9 meters. For model construction, the high spatiotemporal resolution advantage of CYGNSS data was innovatively integrated with the stable observational characteristics of FY-3E data through a wavelet transform-based fusion approach, achieving complementary observational benefits. Validation against the DTU mean sea surface model indicates that the final fused product achieves a mean absolute error of 0.93 meters, representing an improvement of approximately 48% compared to the single-source CYGNSS physical retrieval method. This outcome provides additional data support for regional marine environment monitoring and research.

Future research will be deepened in the following aspects: (1) More refined tropospheric models and higher spatiotemporal resolution ionospheric products will be adopted to reduce atmospheric delay correction uncertainties at the source; (2) Conducting direct validation against contemporaneous radar altimeter data (e.g., Jason-3, Sentinel-6) to better isolate and quantify the absolute accuracy of the GNSS-R retrievals themselves, distinguishing them from residual dynamic ocean signals present in the DTU21 comparison.

Acknowledgement:

This work was supported by the National Natural Science Foundation of China (41874022), the Basic Research Fund for Central Public Research Institutes (AR2404), and the National Key Laboratory of Spatial Reference (SKLGIE2024-ZZ-7).

References

[1] ZAVOROTNY, U V; GLEASON S; et al. (2014): Tutorial on Remote Sensing Using GNSS Bistatic Radar of Opportunity, [J] IEEE Geoscience and Remote Sensing Magazine, 2014, 2(4): 8-45.

[2] JIN, S G; ZHANG, Q Y; QIAN, X D. (2017): New Progress and Application Prospects of Global Navigation Satellite System Reflectometry (GNSS+R), [J] Acta Geodaetica et Cartographica Sinica, 2017, 46(10): 1389-1398.

[3] SUN, Z M; GUAN, B.; ZHAI, Z. H.; OUYANG, M. D. (2022): Research progress of ocean satellite altimetry and its recovery of global marine gravity field and seafloor topography model, [J] Acta Geodaetica et Cartographica Sinica, 2022, 51(6): 923-934.

[4] MARTIN-NEIRA, M. (1993): A passive reflectometry and interferometry system (PARIS): Application to ocean altimetry, ESA journal, 1993, 17(4): 331-355.

[5] ClARIZIA, M. P.; RUF, C.; et al. (2016): First spaceborne observation of sea surface height using GPS-Reflectometry, [J] Geophysical Research Letters, 2016, 43(2): 767-774.

[6] TIAN L M. (2016): Research on the ocean altimetry with beidou reflection signal (in Chinese) [D]. Shanghai: Shanghai Ocean University, 2016.

[7] MASHBURN, J.; AXELRAD, P.; et al. (2018): Global ocean altimetry with GNSS reflections from TechDemoSat-1, [J] IEEE Transactions on Geoscience and Remote Sensing, 2018, 56(7): 4088-4097.

[8] LI, W. Q.; CARDELLACH, E.; et al. (2019): Assessment of Spaceborne GNSS-R Ocean Altimetry Performance Using CYGNSS Mission Raw Data, [J] IEEE Transactions on Geoence and Remote Sensing, 2019, 58(99):238-250.

[9] MASHBURN, J.; AXELRAD, P.; et al. (2020):

Improved GNSS-R ocean surface altimetry with CYGNSS in the seas of Indonesia, [J] IEEE Transactions on Geoscience and Remote Sensing, 2020, 58(9): 6071-6087.

[10] ZHANG, Y.; MA, D. H.; et al. (2021): Sea surface height inversion of GPS reflected signal based on TechDemoSat-1 satellite, Journal of Beijing University of Aeronautics and Astronautics, 2021, 47(10): 1941-1948.

[11] QIU, H. and JIN, S. (2020): Global mean sea surface height estimated from spaceborne cyclone-GNSS reflectometry, [J] Remote Sensing, 2020, 12(3): 356.

[12] ZHANG, Y.; LU, Q.; et al. (2023): Global sea surface height measurement from CYGNSS based on machine learning, IEEE Journal of Select ed Topics in Applied Earth Observations and Remote Sensing, 2023, 16:841-852.

[13] CHENG Z, JIN T, CHANG X, et al. Evaluation of spaceborne GNSS-R based sea surface altimetry using multiple constellation signals, [J] Frontiers in Earth Science, 2023, 10: 1079255.

[14] ZHANG, Y.; LU, Q.; et al. (2025): Spaceborne GNSS-R sea surface height inversion model using FY-3E, Journal of Beijing University of Aeronautics and Astronautics，2025，51（10）：3262-3272.

[15] ZHANG, Y.; ZHENG, W. and LIU, Z. (2024): Improving the spaceborne GNSS-R altimetric precision based on the novel multilayer feedforward neural network weighted joint prediction model, [J] Defence Technology, 2024, 32: 271-284.

[16] XING, J.; YANG, D.; et al. (2024): Advancing Sea Surface Height Retrieval through Global Navigation Satellite System Reflectometry: A Model Interaction Approach with Cyclone Global Navigation Satellite System and FengYun-3E Measurements, [J] Remote Sensing, 2024, 16(11): 1896.

[17] ZUFFADA, C.; LI, Z. J.; et al. (2015): The Rise of GNSS Reflectometry for Earth Remote Sensing [C]//IEEE International Geoscience and Remote Sensing Symposium, Milan, Italy, 2015.

[18] Clarizia, M. P. and C. S. Ruf (2016): Wind Speed Retrieval Algorithm for the Cyclone Global Navigation Satellite System (CYGNSS) Mission, [J] IEEE Transactions on Geoscience and Remote Sensing, 2016, 54(8): 4419-4432.

[19] CHEN, D. and DONG, Z. N. (2025): Soil Moisture Retrieval Based on FY-3E GNOS Reflection Measurement [J], Journal of Geodesy and Geodynamics, 2025, 45(10): 1037-1042.

[20] CARDELLACH, E.; RIUS, A.; et al. (2014): Consolidating the Precision of Interferometric GNSS-R Ocean Altimetry Using Airborne Experimental Data, [J] IEEE Transactions on Geoscience and Remote Sensing, 2014, 52: 4992-5004.

[21] MASHBURN, J.; AXELRAD, P.; et al. (2017): An Assessment of the Precision and Accuracy of Altimetry Retrievals for a Monterey Bay GNSS-R Experiment [J]. IEEE Journal of Selected Topics in Applied Earth Observations & Remote Sensing, 2017, 9(10):4660-4668.

[22] FAN, D.; LI, S. S.; et al. (2017): Altimetry Waveform Retracking Algorithm Comparing for Jason-2 [J].Hydrographic Surveying and Charting, 2017, 37(6): 5-8,16.

[23] Yan, Z.; Zheng, W.; et al. (2022): Correction of atmospheric delay error of airborne and spaceborne GNSS-R sea surface altimetry, [J] Frontiers in Earth Science, 2022, 10: 730551.

[24] Liu, H. (2020): Research on global ionosphere modeling based on multi-source data fusion, [D] Xi'an University of Science and Technology, 2020.

[25] NIELL, A. E. (1996): Global mapping functions for the atmosphere delay at radio wavelengths, Journal of Geophysical Research: Solid Earth, 1996, 101(B2): 3227-3246.

[26] HU, C. J.; BENSON, C. R.; et al. (2019): Impact of receiver dynamics on space-based GNSS-R altimetry, IEEE Journal of Selected Topics in Applied Earth Observations and Remote Sensing, 2019, 12(6) : 1974-1980.

[27] Andersen, O. B.; Rose, S. K.; et al. (2023): The DTU21 global mean sea surface and first evaluation, Earth Syst. Sci. Data, 2023, 15, 4065–4075[EB/OL].

[28] Abdallah, M.; Abd, E. G. R.; et al. (2022): Comparison of recently released satellite altimetric gravity models with shipborne gravity over the Red Sea [J].The Egyptian Journal of Remote Sensing and Space Sciences, 2022, 25(2): 579-592.

[29] Tomić, M.; O. Baltazar Andersen (2023): ICESat-2 for Coastal MSS Determination—Evaluation in the Norwegian Coastal Zone, [J] Remote Sens. 2023, 15(16): 3974.

[30] RUF, C.; McKague, Darren; et al. (2022): CYGNSS Handbook, 2022, www.fucrum.org/concern/monographs/.

[31] Mashburn, J.; O'Brien, A.; et al. (2018): A comparison of waveform model re-tracking methods using data from CYGNSS [C]//IGARSS 2018-2018 IEEE International Geoscience and Remote Sensing Symposium. IEEE, 2018: 4289-4292.

[32] Hu, C.; Benson, C. R.; et al. (2020): The validation of the weight function in the leading-edge-derivative path delay estimator for space-based GNSS-R altimetry, [J] IEEE Transactions on Geoscience and Remote Sensing, 2020, 58(9): 6243-6254.

[33] Rius, A.; Cardellach, E. and Martin-Neira, M. (2010): Altimetric analysis of the sea-surface GPS-reflected signals, [J] IEEE Transactions on Geoscience and Remote Sensing, 2010, 48(4): 2119-2127.

[34] Park, H.; Camps, A.; et al. (2012): Retracking considerations in spaceborne GNSS-R altimetry, [J] GPS solutions, 2012, 16(4): 507-518.

Authors

Fanfan Xu is a master's degree student at the State Key Laboratory of Spatial Datum, Chinese Academy of Surveying and Mapping, where her research focuses on modeling of vertical reference for the seafloor.

Baogui Ke received his Ph.D. from Wuhan University, China, 2009, and is currently a Professor at Chinese Academy of Surveying and Mapping. His research interest focuses on refined modeling of ocean gravity and vertical datum.

Jinxin Hu is a master’s student, with research interests focusing on tidal simulation and water level correction.

Yuxuan Tan is a candidate for Master's degree at the State Key Laboratory of Spatial Datum, Chinese Academy of Surveying and Mapping, research direction: submarine topography.